

Energy spectra due to the intrinsic radiation of LYSO/LSO scintillators for a wide range of crystal sizes

Dalia Yvette Domínguez-Jiménez

Facultad de Ciencias, Universidad Nacional Autónoma de México, 04510 Mexico City, Mexico

Héctor Alva-Sánchez^{a)}

Instituto de Física, Universidad Nacional Autónoma de México, A.P. 20–364, 01000 Mexico City, Mexico

(Received 4 August 2020; revised 22 October 2020; accepted for publication 21 December 2020; published 1 March 2021)

Purpose: Most detectors in current positron emission tomography (PET) scanners and prototypes use lutetium oxyorthosilicate (LSO) or lutetium yttrium oxyorthosilicate (LYSO) scintillators. The aim of this work is to provide a complete set of background energy spectra, due to the scintillator intrinsic radioactivity, for a wide range of crystal sizes.

Methods: An analytical model, developed and validated in a previous work, was used to obtain the background energy spectra of square base cuboids of different dimensions. The model uses the photon absorption probabilities of the three gamma rays (88, 202, and 307 keV) emitted following the beta decay of ^{176}Lu to ^{176}Hf excited states. These probabilities were obtained for each crystal size considered in this work from Monte Carlo simulations using the PENELOPE code. The probabilities are then used to normalize and shift the beta spectrum to the corresponding energy value of the simultaneous detection of one, two, or three gamma rays in the scintillator. The simulated cuboids had side lengths of 5, 10, 20, 30, 40, 50, and 60 mm and crystal thickness $T = 2.5, 5, 10, 15,$ and 20 mm. From these results a complete set of energy spectra, including intermediate dimensions, were obtained. In addition, LYSO and LSO were compared in terms of their analytical background energy spectra for two crystal sizes. The analytical spectra were convolved using a variable Gaussian kernel to account for the energy resolution of a typical detector. A parameterization of the photon absorption probabilities for each gamma ray energy as a function of the cuboid volume to surface area ratio was obtained.

Results: A data set of L(Y)SO background energy spectra was obtained and is available for the reader as 2D histograms. The model accurately predicts the structure of the energy spectra including the relative peak and valley intensities. The data allow visualizing how the structure evolves with increasing crystal length and thickness. Lutetium yttrium oxyorthosilicate and LSO present very similar background energy spectra for the range of sizes studied in this work and therefore the data generated can be confidently used for both scintillator materials. The filtered spectra showed a variable shift in the main peaks, depending on crystal size, alerting that to achieve a correct detector calibration using the background spectrum is not straight forward and requires precise data analysis and measurements. In addition, we found that square base L(Y)SO cuboids with same volume to surface area ratio have background spectra with the same structure.

Conclusions: We present the energy spectra of L(Y)SO crystal of different sizes which will be very useful for industry and research groups developing and simulating detectors for positron imaging applications in terms of calibration, quality assurance, crystal maps, detector fine gain tuning, background reduction and other applications using the long-lived ^{176}Lu source. We analyzed the data produced in this work and found that crystal cuboids with equal volume to surface area ratio produce the same background energy spectra, a conclusion that simplifies its calculation and clarifies why the same energy spectrum is observed under different experimental setups. © 2021 American Association of Physicists in Medicine [https://doi.org/10.1002/mp.14729]

Key words: background spectrum, detector development and evaluation, intrinsic radioactivity, LYSO, PET detector

1. INTRODUCTION

Ongoing efforts to improve image quality and performance of positron emission tomography (PET) scanners and organ-specific positron imaging systems are aimed at augmenting the system sensitivity, increasing the coincidence time

resolution (CTR) to incorporate precise time-of-flight (TOF) information, refining spatial resolution and ameliorating the drawbacks due to the detection of unwanted random and scattered events. Improvements in these factors have been achieved through the combined advances in both detector technology and the development of newer scanner

architectures. Likewise, advances in correcting for other physical processes, such as positron range, which can be a source of resolution degradation,¹ and motion correction methods² have been included at the reconstruction stage. The ultimate goal is to make PET imaging more quantitative and therefore to make it a better tool for diagnosis and patient follow-up.

The majority of PET detectors rely on the use of scintillator crystals coupled to photodetectors in a two-step detection process. In early PET scanners, bismuth germanium oxide (BGO) was the scintillation material of choice because of its high detection efficiency. However, the incorporation of more precise TOF to better determine the electron-positron annihilation location within the patient has promoted the use of newer scintillator materials with faster timing properties and higher light outputs. By 2010 almost all new systems were based on lutetium oxyorthosilicate (LSO) or lutetium yttrium oxyorthosilicate (LYSO) scintillators owing to its good light yield with a short decay time, offering better timing capabilities and good energy resolution for photon discrimination, while having a high effective atomic number and physical density providing a high intrinsic detection efficiency for 511 keV annihilation photons. Better timing properties of the scintillation process were matched by the gradual replacement of photomultiplier tubes with state-of-the-art silicon photomultiplier (SiPM) detectors, with a faster timing response, a high photon detection efficiency and low noise.³ With the combination of L(Y)SO + SiPM technology, the timing resolution has been reduced to a few hundred picoseconds achieving improved resolution as a result of the incorporation of TOF information during the reconstruction processes. The target of reducing the CRT to 10 ps in clinical scanners, a point where image reconstruction will be no longer necessary, remains an important challenge.

System sensitivity in clinical PET has been also increased by expanding the dimensions of the scanners along the axial direction to cover a larger portion of the human body, including total body scanners capable of scanning the total length of a patient simultaneously.^{4,5} This increases the system sensitivity due to larger solid angle coverage and also by an increased length of the scintillator material for photons traveling in very oblique directions. Yet, this poses additional difficulties, not only in terms of the number of signals and information to be processed due to an increase in the number of detectors and electronics required, but also in terms of better determining the depth-of-interaction and to deal with an increase in photon attenuation inside the patient at oblique lines-of-response. In addition, an improved timing resolution is achieved by using thinner scintillation crystals,⁶ at the expense of a lower detection efficiency. Although many PET detector blocks in commercial scanners use pixelated crystal arrays, various research groups have achieved good performance results using monolithic crystals in terms of spatial resolution, together with the incorporation of depth-of-interaction information by analyzing the scintillation light distributions reaching the photodetectors.^{7–9} All these effects have encouraged research groups to perform simulation studies to

optimize the number of scintillation crystals and the crystal thickness in different detector and scanner architectures.¹⁰

In addition, L(Y)SO scintillation crystals contain the long-lived radioactive isotope ^{176}Lu (3.76×10^{10} yr half-life) producing a constant background signal owing to the self-detection of the beta particles emitted through its decay to ^{176}Hf and the simultaneous detection of one, two, or three gamma rays from the excited states of the daughter nucleus. This intrinsic radioactivity produces a count rate of approximately 300 cps per cm^3 in singles mode and an energy spectrum with a distinctive structure reported by several research groups.^{11–14} The underlying physical mechanisms responsible for its peculiar structure, which depends on the crystal size, were explained by an analytical model developed by our group. The model combines the probabilities of the gamma ray/internal conversion electron emissions from the ^{176}Lu to ^{176}Hf decay scheme,¹⁵ the probability of one or more of the gamma rays being detected in a crystal of a particular size, the calculation of the combined probability of gamma emission + gamma ray detection for each particular combination of the gamma rays detected and the shift of the normalized energy spectrum of the beta particles to the deposited energy value.¹⁶ The analytical calculations provide a very accurate prediction of the energy spectra in terms of the maximum energy value and the relative intensities of the observed peaks and valleys as previously validated with experiment¹⁶ and using Monte Carlo simulations.¹⁷

The analytical model developed to predict the background energy spectra works for pixelated crystal arrays, despite that the individual crystal elements are optically isolated from each other. This is true as long as the scintillation light of the complete crystal array is collected by the photodetector. This can be understood by picturing a ^{176}Lu β -particle emitted in a given crystal pixel producing light. Gamma rays/internal conversion electrons from the ^{176}Hf transitions can be detected simultaneously in the same detector block, in the same or different crystal pixels simultaneously, and therefore the shifting and normalizing of the β^- spectrum can be done as prescribed by the model producing the energy spectrum corresponding to the full size crystal. This can be verified from a crystal map, obtained with the background energy spectrum, using a region of interest of any size, even the size of a single crystal, and the resulting energy spectrum will reflect that of the large crystal. Consequently, the crystal is treated by the model as a single monolithic block (neglecting photon attenuation in the thin, a few microns thick walls separating individual elements). At regions near the crystal edges, however, the background spectrum may appear distorted as a result of a higher probability of escaping gamma rays and due to the specific detector readout method used.

The energy spectra from this model still needs to consider the finite energy resolution of the specific detector used, which can be introduced by convolving the analytical spectrum with a variable normalized Gaussian function reflecting the measured energy resolution as a function of the energy.¹⁶ The fact that this model reproduces the main features of the background energy spectra, without the inclusion of optical

processes of the scintillation light, indicates that the radiation decay and detection physics are the dominating processes over other factors (e.g., properties of the crystal wrapping material, scintillation light absorption, photon detection efficiency, and linearity of the photodetector) which need to be taken into consideration if a more realistic energy spectrum is required. More recently, this model has been extended to understand the energy spectra for a pair of LYSO crystals working in coincidence mode due to the intrinsic radioactivity, with predictions in good agreement with Monte Carlo simulations and experiments.¹⁸

Monte Carlo simulations can also be used to obtain the energy spectra for a particular crystal size, as shown in the work by Enríquez-Mier-y-Terán et al.,¹⁷ who used Geant4 Application for Tomographic Emission (GATE) v8.1.¹⁹ Monte Carlo simulations produce more accurate energy spectra since Compton scattered photons escaping from the crystal, depositing a fraction of the gamma ray energy, are not considered in the analytical model. In that work, the energy spectra for crystal cuboids of thickness 10 mm and six different lengths (10, 20, 30, 40, 50, and 57.4 mm) were obtained and compared to the analytical model predictions, showing that the model is able to reproduce with a high degree of accuracy, with a better agreement for increasing crystal length, the spectra for other crystal sizes. However, simulations of the complete decay and detection processes using GATE or other simulation packages can be time consuming and require an experienced user to correctly set the involved simulation parameters to obtain the correct energy spectrum.

In many clinical scenarios, the background count rate can be negligible compared to the activity being imaged. In some cases, however, when imaging low activity values or when the number of crystals in an imaging system is large, as in the case of total-body scanners, dealing with the background counts can be more exigent. Some research groups have examined the effect that ¹⁷⁶Lu background has on the imaging of very low activity sources in preclinical²⁰ and in clinical

PET scanners²¹ and recently one group has used machine learning algorithms to reduce it.²² Notwithstanding, the crystal intrinsic radiation has been also proposed to be used for convenient applications including transmission scans.²³

The detailed knowledge of this background energy spectrum in singles mode can have technological applications including detector calibration²⁴ and detector performance assessment in terms of counting rate and energy resolution without the need of external sources, detector routine quality control for fine tuning detector gain,^{25,26} energy window setting, among others. Since the structure of the background energy spectra depends on crystal size, in this work we have calculated the detection probabilities required to compute the analytical energy spectra for a range of crystal sizes typically used in current PET and other imaging detectors using LYSO using the analytical calculations.

Tables I and II list examples of clinical and preclinical PET scanners and systems, respectively, that use pixelated L(Y)SO crystal arrays in their detector modules. In the tables, the detector module size refers to the area where the scintillation light is shared at the photodetector readout level. Table III lists some clinical and preclinical systems that incorporate monolithic LYSO crystals. There are also numerous published works on individual PET detector development and evaluation which use an even wider range of crystal sizes and to mention all the individual advances in PET detector technology would be a colossal task, more appropriate for a review paper. Therefore, these tables are not intended to be exhaustive, but are an attempt to give specific examples to show the wide range of L(Y)SO crystal sizes and geometries used in detector blocks of current PET systems and consequently to justify the crystal sizes considered in this work.

The aim of this work is to provide a complete set of L(Y)SO background energy spectra for a wide range of crystal sizes covering the dimensions used by the majority of PET scanners and systems, and from the data to extract general patterns and conclusions.

TABLE I. Clinical systems using L(Y)SO pixelated crystal arrays.

Project/developer	System type	Detector module size (mm × mm)	Crystal thickness (mm)	Crystal array	Crystal pixel size (mm × mm)	Reference
1 mm ³ resolution clinical PET system	Organ specific (brain, breast)	7.2 × 7.2	1.0	8 × 8	0.9 × 0.9	[27]
PEM system, University of Texas	Breast dedicated	18.48 × 18.48	10	12 × 12	1.54 × 1.54	[28]
PEM Flex Solo II, Naviscan	Breast dedicated	26 × 26	13	13 × 13	2 × 2	[29]
Breast-PET/CT scanner, West Virginia University	Breast dedicated	48 × 48	15	24 × 24	2 × 2	[30]
PennPET, University of Pennsylvania	Total Body	3.86 × 3.86	19	1 × 1 ^a	3.86 × 3.86	[5]
MR insertable brain PET Sogang University	Brain dedicated	12 × 12	20	4 × 4	3.0 × 3.0	[31]
Siemens Biograph (TPTV, mCT, mCT Flow 64-4R PET/CT)	Whole Body	52 × 52	20	13 × 13	4 × 4	[32–34]
Siemens Biograph vision PET/CT	Whole Body	16 × 16	20	5 × 5	3.2 × 3.2	[35]

^aThese detectors use 1:1 coupling of the individual crystal pixels with the photodetector.

TABLE II. Preclinical systems using L(Y)SO pixelated crystal arrays.

Project	Detector module size (mm × mm)	Crystal thickness (mm)	Crystal array	Crystal pixel size (mm × mm)	Reference
Matrix9 UC Davis	12 × 12	6	8 × 8	1.5 × 1.5	[36]
Concorde Microsystems/Siemens Focus 120	18 × 18	10	12 × 12	1.5 × 1.5	[37]
Concorde Microsystems/Siemens microPET P4	17.6 × 17.6	10	8 × 8	2.2 × 2.2	[38]
ClearPET, Crystal Clear Collaboration	16 × 16	10	8 × 8	2.0 × 2.0	[39]
Siemens Inveon	30 × 30	10	20 × 20	1.5 × 1.5	[40]
Small-animal Hyperion IID PET/MRI insert	27.9 × 27.9	12	30 × 30	0.93 × 0.93	[41]
VrPET SEDECAL	42 × 42	12	30 × 30	1.4 × 1.4	[42]

TABLE III. PET systems using monolithic L(Y)SO crystals.

Project	System type	Crystal size (mm × mm)	Thickness (mm)	Reference
MOLECUBES	Preclinical small animal	25.4 × 25.4	8	[43]
β-CUBE	Preclinical small animal	50 × 50	8	[44]
ALBIRA	Preclinical small animal SPECT/PET/CT	40 × 40, 50 × 50 ^a	10	[45]
MAMMI	Clinical dedicated breast imaging	40 × 40, 50 × 50 ^a	10	[46]
Preclinical total-body PET/CT scanner	Preclinical small-animal	48 × 48, 50 × 50 ^a	10	[47]
MINDView	Clinical Dedicated brain	50 × 50	20	[48]
Dual-sided DPC PET detector	Clinical PET detector	32 × 32	22	[49]

^aTruncated pyramid, the values give the size of the parallel planes.

2. MATERIALS AND METHODS

2.A. LYSO energy spectra for different crystal sizes

The analytical model used to obtain the energy spectra was explained in detail in Ref. [16] and its accuracy has been verified by comparing its predictions to experimental data and to Monte Carlo simulations, which include all radiation emission and detection mechanisms involved. Briefly, the model assumes that in a long observation period, for example, the time required to acquire an energy spectrum with sufficient statistics, many beta particles are emitted from the decay ^{176}Lu to ^{176}Hf . In this model, the complete energy spectra of the beta particles, data obtained from Ref. [50], are shifted to the correct higher energy value to account for the simultaneous detection of the beta particle and one, two or all three gamma rays or internal conversion electrons, arising from the isomeric transitions of the excited states of

^{176}Hf , considering their emission probabilities from its decay scheme.¹⁵ We introduced into the analytical model a 6.9% internal conversion decay process associated with the 307 keV isomeric transition in the ^{176}Hf excited states as reported in the Nuclear Data Sheets for $A = 176$ by M.S. Basunia.⁵¹ To obtain the probability of detection of each gamma ray, Monte Carlo simulations were performed using PENELOPE.⁵² In the simulations, isotropic, point-like sources of monoenergetic photons are generated inside the LYSO crystal volume. For each crystal geometry three simulations are required: one for each gamma-ray energy value. The simulations provide the fraction of events in which all the photon energy is deposited in the crystal to the total number of generated photons. Particles are assumed to be stopped and absorbed in the medium when their energy is equal to or below 10 keV. Events in which secondary (scattered) photons escape from the crystal, so that only part of the original energy is deposited, are not included in the model. Although this limits the accuracy of the calculation, the fraction of scattered photons escaping the crystal is small¹⁷ and the model gives very accurate predictions of the energy spectra. These simulations are relatively simple to setup and take a relatively short time (~10 min for 1 million primary photons) to complete in a present-day desktop computer.

The simulated crystal geometries were square base cuboids with side lengths $L = 5, 10, 20, 30, 40, 50$, and 60 mm and crystal thickness $T = 2.5, 5, 10, 15$, and 20 mm, thus a total of 105 simulations were performed: three gamma ray energies in 35 crystal sizes. All simulated crystals were LYSO with physical density of 7.1 g/cm³ with elemental composition shown in Table IV. The crystal dimensions were chosen to cover most of the crystal sizes used in clinical and preclinical PET scanners (Tables I–III).

The probabilities obtained from the Monte Carlo simulations were plotted separately as a function of L and T . For each gamma ray energy value, fittings to the curves of the following form were generated:

$$P(L) = a_1 (1 - e^{-a_2 L}) \quad (1)$$

$$P(T) = b_1 (1 - e^{-b_2 T}), \quad (2)$$

TABLE IV. $\text{Lu}_{1.8}\text{Y}_{0.2}\text{SiO}_5\text{:Ce}$ (LYSO) and $\text{Lu}_2\text{SiO}_5\text{:Ce}$ (LSO) elemental composition. Atomic mass values from Ref. [53].

Element	Atomic mass (u)	Number of atoms in molecule		Total mass (u)		Fraction	
		LSO	LYSO	LSO	LYSO	LSO	LYSO
Lu	174.97	2	1.8	349.94	314.95	0.7640	0.7145
O	16.00	5	5	80.00	80.00	0.1747	0.1815
Si	28.09	1	1	28.09	28.09	0.0613	0.0637
Y	88.91	0	0.2	0.00	17.78	0.0000	0.0403
		Total		458.02	440.81	1.00	1.00

where a_1 , a_2 , b_1 and b_2 are the fitting coefficients. This form was chosen since it resembles the expression for the intrinsic efficiency of a material for a narrow photon beam. The situation here is quite different, since the sources are uniformly located inside the crystal volume. Still, this expression produces a good fitting to the data.

From the fitting coefficients, the probability values of intermediate dimensions, evaluated every millimeter, were obtained and plotted in a two-dimensional (2D) histogram for each photon energy. The fitted curves produced better results than simple bilinear interpolation. We also tried a surface fitting (2D function) to the data of the form $P(L, T) = k(1 - e^{-aL})(1 - e^{-bT})$, with k , a and b the fitting parameters. Although reasonably good, the fitting is not as accurate as the previously mentioned, when comparing the $P(L, T)$ computed values to those obtained directly from the Monte Carlo simulations.

Using the calculated probability values obtained with the functions in Eqs. (1) and (2), the energy spectra were obtained for each simulated crystal thickness T for length values $L = 1$ to 60 mm, every millimeter. Therefore, for each T value, a 2D image containing the energy spectra (x -axis) for all crystal lengths (y -axis) were produced. Each image is of size 1200 pixels (1 pixel = 1 keV) in length by 60 pixels (1 pixel = 1 mm) wide. Images were generated with a linear grayscale colorbar, whose intensity reflects each energy value. Thus, if a horizontal 1-pixel thick profile is taken across the full length (1200 pixels) of the image, the corresponding energy spectrum is obtained.

2.B. LYSO vs LSO

Although LSO and LYSO have a very similar elemental composition and density, to compare the background energy spectra due to both scintillation materials, the analytical calculations, including the simulation of monoenergetic photons in LSO crystals, were performed for two crystal sizes: 10 mm cube and a square base cuboid with side length of 57.4 mm and thickness 10 mm. The elemental composition of LSO is listed in Table IV and its physical density was taken as 7.4 g/cm³. The photon mean free path, fraction of Compton/photoelectric interactions, and crystal length required to absorb (intrinsic efficiency) 99% of 88, 202, 307, and 511 keV photons for both materials are listed in Table V.

2.C. Filtering of energy spectra

To take into account the finite energy resolution of the complete detector (scintillation crystal + photodetector), the analytical spectra can be convolved with a Gaussian of variable width to reflect the fact that the energy resolution is a function of the energy E itself. If the detector is governed by Poisson statistics, then the energy resolution is proportional to $E^{-1/2}$ as derived in Ref. [55]. This filtering method was successfully applied previously using variable normalized Gaussian functions whose width, given by the standard deviation σ , varied with the photon energy E as $\sigma(E) = 1.15E^{0.52}$ keV, which reflected the energy resolution of a particular detector module as obtained experimentally with a set of external radioactive sources.¹⁶ Here we used the same variable Gaussian kernel to demonstrate the effect the filtering has on the analytical spectra. Naturally, the energy resolution and its dependence on photon energy will depend on the particular detector block arrangement (crystal + photodetector).

3. RESULTS

3.A. Photon absorption probabilities for different crystal sizes

Figure 1 shows the photon absorption probability as a function of crystal length and thickness for the three gamma

TABLE V. Photon detection properties for LSO and LYSO scintillation crystals, data from Ref. [54].

Photon energy (keV)	Fraction Compton/photoelectric		Mean free path (cm)		Crystal length (cm) for intrinsic efficiency = 0.99	
	LSO	LYSO	LSO	LYSO	LSO	LYSO
88	0.028/0.972	0.029/0.971	0.0313	0.0344	0.144	0.158
202	0.190/0.810	0.200/0.800	0.2406	0.2624	1.108	1.208
307	0.389/0.611	0.404/0.596	0.5561	0.5996	2.561	2.761
511	0.658/0.342	0.672/0.328	1.1520	1.2216	5.305	5.625

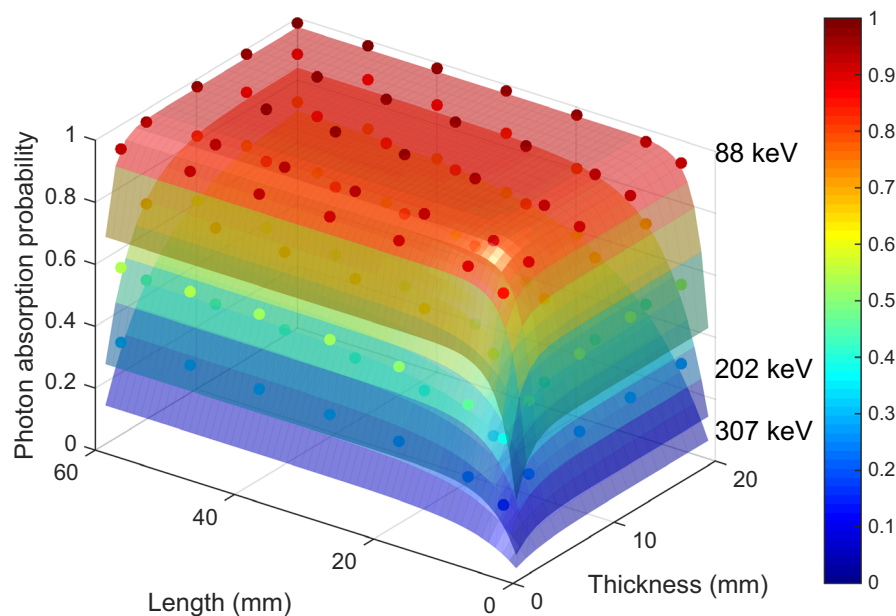


FIG. 1. Photon absorption probabilities for square base crystal cuboids of varying lengths and thicknesses. The symbols represent the values obtained directly from Monte Carlo simulations and the surfaces were obtained by fitting functions from Eqs. (1) and (2). [Color figure can be viewed at wileyonlinelibrary.com]

ray energies of the ^{176}Lu decay. The plot is the result of the 2D calculation of the fitting functions [Eqs. (1) and (2)]. The round symbols represent the data of the actual Monte Carlo simulation results. From this figure one can observe that the absorption probabilities for 88 keV photons are always larger than the probabilities for 202 keV photons, which in turn, are larger for the 307 keV photons, as expected. Also, the probability values fall with decreasing crystal length and thickness. The maximum photon absorption probability for 88, 202, and 307 keV photons are 0.986, 0.883, and 0.729, respectively, which correspond to $L = 60$ mm and $T = 20$ mm, the three points located at the back corner of the figure. The smallest photon absorption probabilities, for $L = 2.5$ and $T = 5$ mm were 0.852, 0.382, and 0.169 for photon energies of 88, 202, and 307 keV, respectively. The probability values were used in the model to compute the energy spectra of LYSO crystals of thickness $T = 2.5, 5, 10, 15$, and 20 mm for crystal lengths from 1 to 60 mm, every mm (Section 3.B). These probability values will become very relevant in Section 4.

3.B. LYSO energy spectra for different crystal sizes

The complete set of the analytical energy spectra, for $L = 1$ to 60 mm, are included on the left of Fig. 2 for two crystal thicknesses: $T = 5$ mm (top) and $T = 20$ mm (bottom). The spectrum intensity (y-axis) reflects the probability per unit keV, such that the integral of each energy spectrum equals unity. These figures show the evolution of the characteristic structure of the spectra with crystal length. Indicated in the figure are the energy values of the most prominent peaks at 88 keV, $88 + 202 = 290$ keV, $88 + 307 = 395$ keV, and $88 + 202 + 307 = 597$ keV. To the right of the energy spectra the intensities of the prominent peaks are

plotted as a function of L to ease visualization of energy spectra progression. For instance, the intensity of the peak at 597 keV grows with increasing crystal length owing to a higher probability of the simultaneous detection of all three gamma rays within the crystal. Also, as this probability grows with increasing L , the probability of the other gamma ray detection combinations fall asymptotically. This probability is also larger for thicker crystals compared to thinner cuboids. In other words, these curves give the relative peak intensities for all lengths of LYSO square base cuboids of a given thickness.

Figure 3 contains 2D histograms of the analytical energy spectra of square base LYSO cuboids for different thicknesses T . Each 2D histogram is 60 pixels wide, corresponding to crystal lengths $L = 1$ to 60 mm (1 pixel in y direction = 1 mm) and 1200 pixels long (1 pixel in x direction = 1 keV). The pixel intensity reflects the probability values per keV; all five images share the same common colorbar on the right. Therefore, if a 1-pixel line profile is taken horizontally across an image the corresponding energy spectrum is retrieved. The sum of the pixel values of each energy spectrum (each horizontal profile) equals 1. The sharp discontinuities correspond to the peak positions. These histograms, with the correct probability values, are available as tiff images as supplementary data and can be downloaded to recover the desired energy spectrum. For example, the energy spectra shown and plots in Fig. 2 can be reproduced directly from the corresponding tiff images.

3.C. LYSO vs LSO

The analytical energy spectra for a small 10 mm cube and a large LSO cuboid ($L = 57.4$ mm, $T = 10$ mm) are plotted together with the analytical energy spectra of LYSO crystals

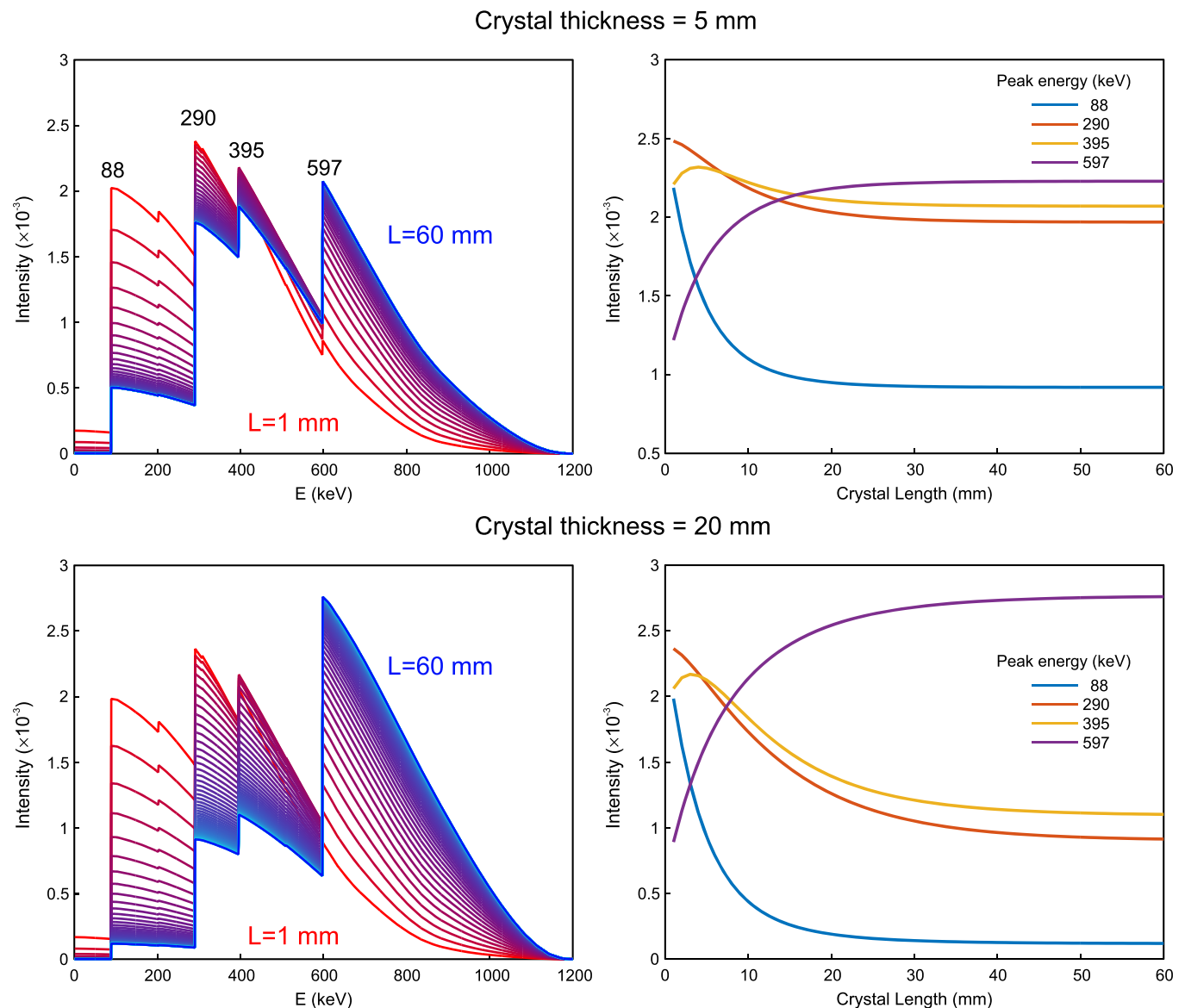


FIG. 2. On the left the energy spectra due to the intrinsic radioactivity of LYSO square base cuboids of lengths $L = 1$ to 60 mm for two different thicknesses, $T = 5$ mm (top) and $T = 20$ mm (bottom). To the right, the intensities of the most prominent peaks are shown as a function of crystal length. [Color figure can be viewed at wileyonlinelibrary.com]

of the same dimensions in Fig. 4. It is evident from this figure that despite the differences, owing to the composition and density of the materials, the energy spectra are essentially the same. Therefore, the results obtained for LYSO crystals (Figs. 2 and 3) can be applied for LSO crystals with a fair degree of accuracy. The higher density and effective atomic number of LSO compared to LYSO results in a higher 597 keV peak intensity for LSO compared to LYSO. These results, however, do not account for the light yield of each material. The amount of scintillation light can be different due to the content of yttrium in LYSO and to the specific doping element, for example, cerium or calcium.⁵⁶ It is the spectrum structure, including the relative peak intensities, that is very similar for both scintillators. In addition, the finite energy resolution of the particular scintillator and photodetector configuration will produce a smoothed spectrum.

3.D. Filtering of energy spectra

Figure 5 shows the result of convolving the analytical energy spectra with a variable Gaussian kernel for LYSO cuboids of fixed length $L = 30$ mm and different crystal thickness. A shift of the peak/valley at 597 keV in the analytical spectra is unmistakably seen to higher/lower energy values. The shift is larger for increasing crystal sizes and can be up to several tens of keV for a large crystal depending on the detector energy resolution. For example, indicated in Fig. 5, for the thickest crystal ($T = 20$ mm) the 597 keV peak appears at approximately 652 keV, a 55 keV difference. This is an effect caused by the convolution of the asymmetric distributions with variable Gaussian function emulating the variation of the energy resolution with the photon energy of a real detector. The peak/valley shifting can be intuitively

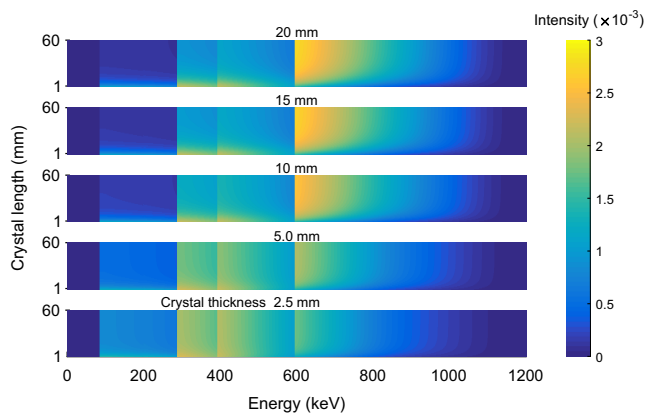


FIG. 3. Two-dimensional histograms containing the analytical energy spectra of LYSO square base cuboids of different thicknesses. The energy spectrum of any length from $L = 1$ to 60 mm can be obtained through a horizontal line profile from a given image. [Color figure can be viewed at wileyonlinelibrary.com]

understood since the convolution of a Gaussian function with an asymmetrical distribution (as the LYSO energy spectra) results in the original distribution smoothed out with a “pulling” or “stretching” of the distribution toward the most intense region. The amount of shift and smoothing of the energy spectra will depend of the particular crystal + photodetector used. Note, however, that the maximum end-point energy at 1190 keV (the Q-value of the decay ^{176}Lu to ^{176}Hf) remains unchained and is an important landmark. The peak shifting as a result of filtering (finite energy resolution) is important, can be observed in background energy spectra published by other research groups,^{14,24,57,58} has led to detector miscalibration in the past, and needs to be taken into account if a correct detector energy assessment is to be attained using the intrinsic background radiation.

4. DISCUSSION

The complete set of background analytical energy spectra of LYSO crystals obtained in this work has prompted us to

search for patterns in different ways. For example, using a simple Monte Carlo code we computed the distribution of distances from points located inside the volume of square base cuboids to points located on the cuboid faces. We compared these distributions (e.g., mean lengths) to the mean free paths of 88, 202, and 307 keV monoenergetic photons in LYSO, and hence to the photon absorption probabilities, with no avail. Another result is that cuboids with the same crystal volume produce dissimilar energy spectra. Surprisingly, we found a simple and extremely useful relation: crystal cuboids with same volume to surface area ratio (V/S) have the same analytical energy spectra.

Figure 6(a), top and bottom, shows the analytical energy spectra for square base cuboids of different dimensions, all of which have the same V/S , equal to 1 and 2 mm, respectively. All spectra are visually very similar, a fact that has been also quantified using the Kullback–Leibler divergence, a measure of how different two probability distributions are Ref. [59]. The small differences can be attributed to the small variations of the probability values obtained from the 2D surface fitting (Fig. 1). This result is at least true for square base cuboids with dimensions in the intervals studied in this work.

The fact that crystals with same V/S ratio have same background spectra could have been anticipated by directly inspecting the photon absorption probabilities calculated from the Monte Carlo simulations. Indeed, cuboids with same V/S have very similar photons absorption probabilities for the three photon energies. To show this fact, in Fig. 6(b) is a plot of the absorption probability for 88, 202, and 307 keV photons as a function of the V/S ratio. Each symbol represents the average value of different crystal sizes with the same V/S : from 0 to 1.25 five values were used, from 1.25 to 2.5 four values were used, from 2.5 to 5, three crystal sizes were used, and from 5 to 6 only two values. These values were found by fixing V/S and the crystal thickness, and hence finding the crystal lengths L from a simple algebraic expression obtained from the geometrical relation of volume to surface area of a square base cuboid. The error bars were chosen as the standard deviation of the values used to calculate the

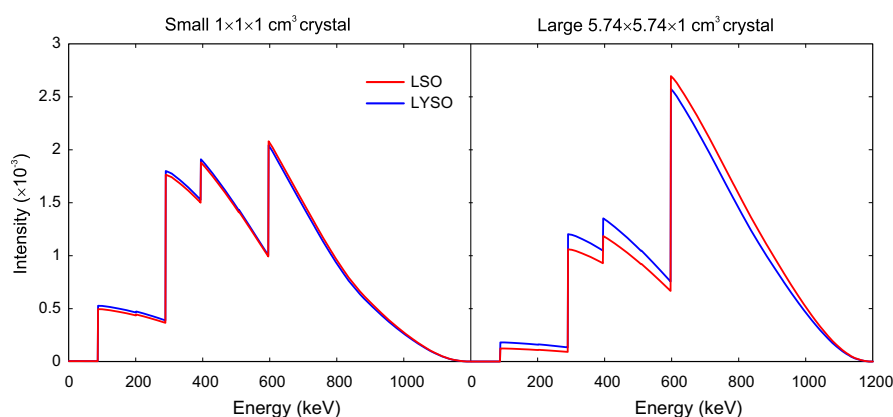


FIG. 4. Analytical energy spectra for LYSO and LSO crystals of two sizes. Left: a small cube 10 mm. Right: a large 10 mm thick square base cuboid. [Color figure can be viewed at wileyonlinelibrary.com]

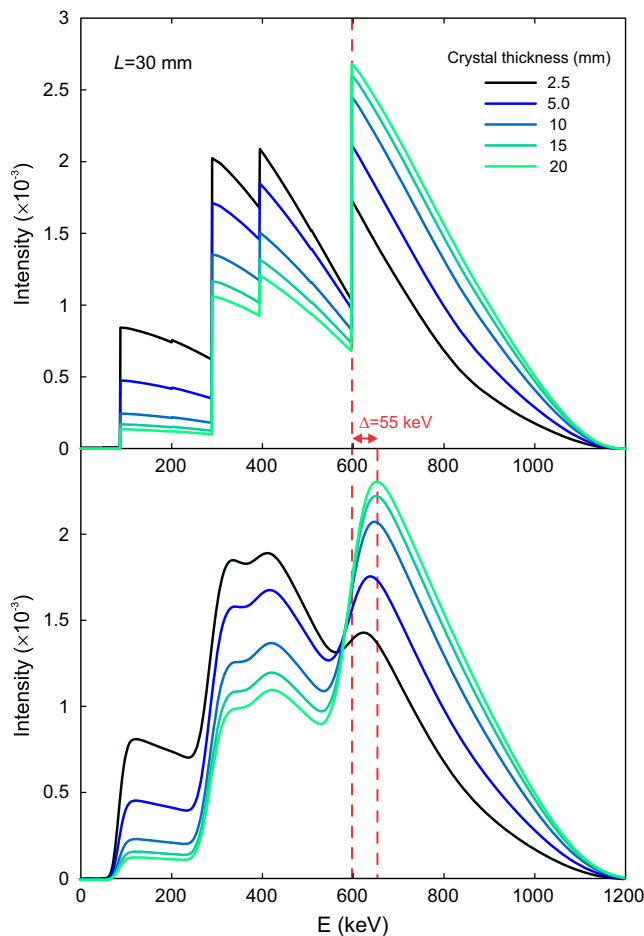


FIG. 5. Analytical (top) and filtered (bottom) energy spectra for square base LYSO cuboids of length $L = 30$ mm and different thicknesses. [Color figure can be viewed at wileyonlinelibrary.com]

mean photon absorption probabilities. The apparent discontinuity in the graph is the result of using a different number of values in each interval. The continuous lines are best fits to the data points of the form:

$$P(V/S) = c_1 \left(1 - e^{-c_2 V/S} \right), \quad (3)$$

where c_1 and c_2 are the fitting coefficients, included in Table VI. This fitting function was chosen due to the inherent tendency of the data to asymptotically reach a maximum value.

Actually, this is all what is needed to compute the background energy spectrum of a square base cuboid of any given length with crystal thickness up to 20 mm without the need to perform Monte Carlo simulations. For a given crystal, the V/S ratio is calculated and the photon absorption probabilities for the three photon energies are evaluated using equation 3 with parameters c_1 and c_2 . These constitute the input the values to the analytical model to normalize and shift the continuous ^{176}Lu beta energy spectrum, and after summing up all the resulting shifted distributions, the final spectrum is obtained.

Perhaps more data and analysis is needed to explain why this conclusion is true. We have compared the inverse values

of c_2 to the photon mean free paths in LYSO (Table V) without success to find a deeper physical reason. Note that the probability values obtained from the simulations are an input to the analytical model, thus the underlying physical processes of the radiation transport/interaction in the crystal of different geometries are the responsible of this finding. Possibly, the V/S result is also valid for cuboids with different lengths, widths, and thicknesses; work is underway to test this extraordinary finding. This result could potentially be extended to other crystal geometries such as monolithic truncated pyramids commonly used in PET scanners that have detectors arranged in rings (see Table III). Further research can also encompass an analysis of more innovative and complex geometries including continuous LYSO crystal tubes^{60,61} to predict the analytical shape of the energy spectrum due to the natural radioactivity.

5. CONCLUSIONS

In this work we have presented the analytical energy spectra due to the intrinsic radioactivity of L(Y)SO scintillation crystal, the most common material used in current clinical and preclinical positron imaging scanners and prototypes. We have calculated the spectra for a wide range of square base cuboid of varying side lengths and thicknesses to cover the most common crystal dimensions used today. The set of energy spectra is available as supplementary data of this paper, available for the reader. These data can be very useful for detector assessment, routine quality control, and as a check for computer simulations of individual or complex detector arrangements that use L(Y)SO crystals.

To account for the energy resolution of a particular detector, the analytical spectrum was convolved with a variable Gaussian function. This revealed that a shift in the position of the main peaks/valleys can be up to a few tens of keV, indicating that care must be exercised when performing detector energy calibration using the background only.

Finally, after computing a wide range of energy spectra and analyzing the complete data set, we found that L(Y)SO square base cuboids with equal volume to surface area ratio have the same background energy spectra due to its intrinsic radioactivity. This conclusion, which needs a systematic experimental verification, removes the need for computing the photon absorption probabilities through Monte Carlo simulations needed for predicting the energy spectra. Also, this conclusion will aid research groups and teams developing PET technology that L(Y)SO scintillators to calibrate and assess detector performance using the constant background radiation and to simply understand why certain crystal sizes produce a particular spectrum, a fact that has puzzled scientists in the past.

ACKNOWLEDGMENTS

None.

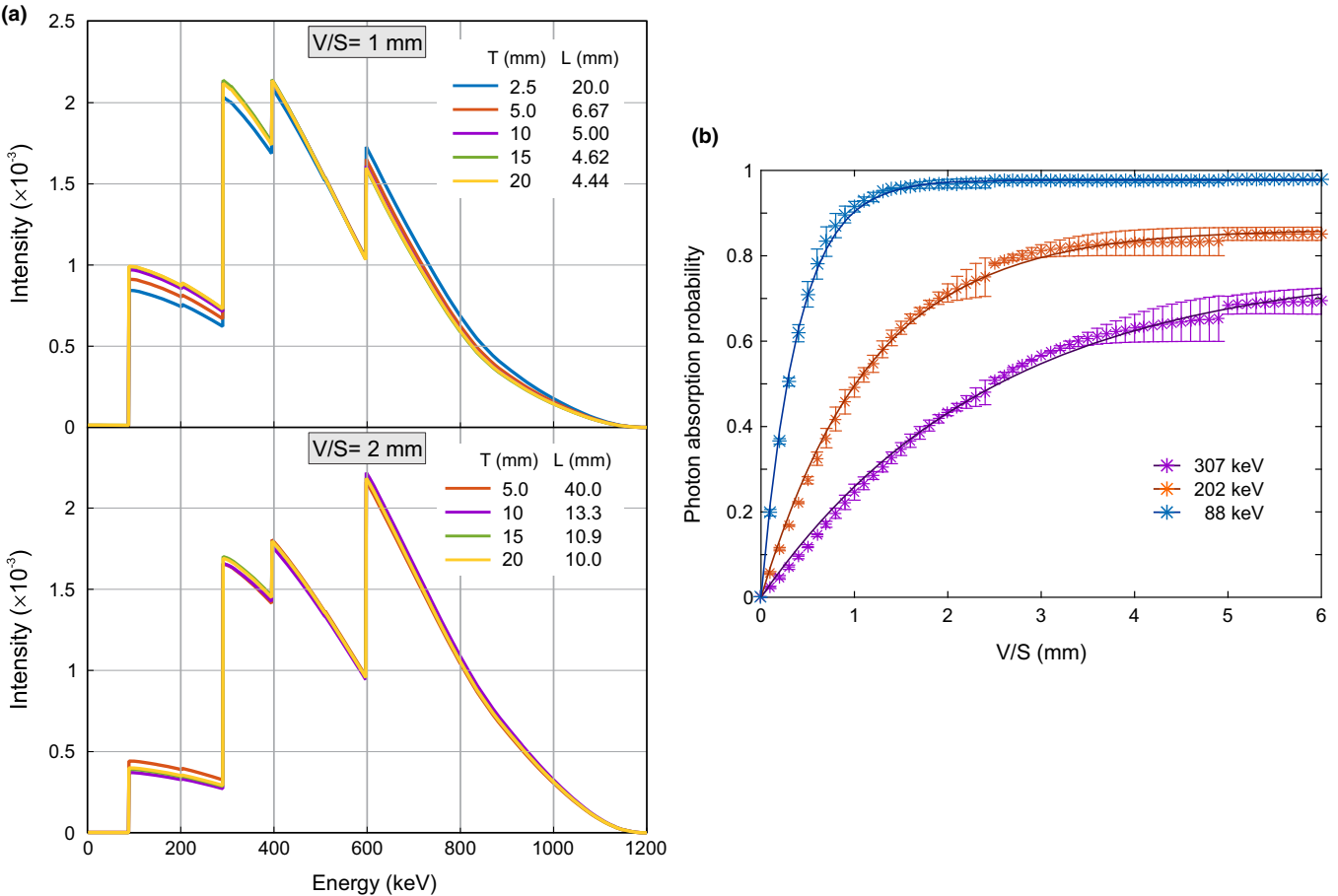


FIG. 6. (a) Energy spectra for different square base LYSO crystals that have the same volume to surface area ratio $V/S = 1$ mm (top) and $V/S = 2$ mm (bottom). (b) Absorption probability for 88, 202, and 307 keV photons as a function of V/S . [Color figure can be viewed at [wileyonlinelibrary.com](#)]

TABLE VI. Best fit coefficients of Eq. (3) to the data plotted in Fig. 6(b).

Photon energy (keV)	c_1	c_2 (mm ⁻¹)
88	0.98	2.57
202	0.86	0.85
307	0.78	0.40

CONFLICT OF INTEREST

The authors declare that they have no conflict of interest.

^{a)}Author to whom correspondence should be addressed. Electronic mail: halva@fisica.unam.mx; Telephone: +52(55)5622-5000.

REFERENCES

1. Cherry SR. The 2006 Henry N. Wagner Lecture: of mice and men (and positrons)—advances in PET imaging technology. *J Nucl Med.* 2006;47:1735–1745.
2. Rahmim A, Rousset O, Zaidi H. Strategies for motion tracking and correction in PET. *PET Clin.* 2007;2:251–266.

3. Ullah MN, Pratiwi E, Cheon J, Choi H, Yeom JY. Instrumentation for time-of-flight positron emission tomography. *Nucl Med Mol Imaging.* 2016;50:112–122.
4. Badawi RD, Shi H, Hu P, et al. First human imaging studies with the EXPLORER Total-Body PET Scanner. *J Nucl Med.* 2019;60:299–303.
5. Karp JS, Viswanath V, Geagan MJ, et al. PennPET explorer: design and preliminary performance of a whole-body imager. *J Nucl Med.* 2020;61:136–143.
6. Gundacker S, Acerbi F, Auffray E, et al. State of the art timing in TOF-PET detectors with LuAG, GAGG and L(Y)SO scintillators of various sizes coupled to FBK-SiPMs. *J Inst.* 2016;11:P08008.
7. González-Montoro A, Sánchez F, Martí R, et al. Detector block performance based on a monolithic LYSO crystal using a novel signal multiplexing method. *Nucl Instrum Methods Phys Res Sect A.* 2018;912:372–377.
8. Pani R, Bettiol M, Preziosi E, et al. A novel method for γ -photons depth-of-interaction detection in monolithic scintillation crystals. *IEEE Trans Nucl Sci.* 2016;63:2487–2495.
9. Preziosi E, Sánchez S, González AJ, et al. Performance study of a PET scanner based on monolithic scintillators for different DoI-dependent methods. *J Inst.* 2016;11:C12076.
10. Vandenberghe S, Moskal P, Karp JS. State of the art in total body PET. *EJNMMI Phys.* 2020;7:35.
11. Conti M, Eriksson L, Rothfuss H, et al. Characterization of ¹⁷⁶Lu background in LSO-based PET scanners. *Phys Med Biol.* 2017;62:3700–3711.
12. Melcher CL, Schweitzer JS. A promising new scintillator: cerium-doped lutetium oxyorthosilicate. *Nucl Instrum Methods Phys Res Sect A.* 1992;314:212–214.

13. Yamamoto S, Horii H, Hurutani M, Matsumoto K, Senda M. Investigation of single, random, and true counts from natural radioactivity in LSO-based clinical PET. *Ann Nucl Med*. 2005;19:109–114.
14. Koba Y, Wakabayashi G, Imamura M, et al. Light output response of LYSO(Ce) crystal to relativistic helium and carbon ions. In: 2007 *IEEE Nuclear Science Symposium Conference Record*. IEEE; 2007:2303–2306. <https://doi.org/10.1109/NSSMIC.2007.4436606>
15. Data Center NN. Chart of Nuclides–Decay Radiation (Upton, NY: Brookhaven National Laboratory). <http://www.nndc.bnl.gov/chart>
16. Alva-Sánchez H, Zepeda-Barrios A, Díaz-Martínez VD, Murrieta-Rodríguez T, Martínez-Dávalos A, Rodríguez-Villafuerte M. Understanding the intrinsic radioactivity energy spectrum from ^{176}Lu in LYSO/LSO scintillation crystals. *Sci Rep*. 2018;8:17310.
17. Enríquez-Mier-y-Terán FE, Alva-Sánchez H, Zepeda-Barrios A, Murrieta-Rodríguez T, Martínez-Dávalos A, Rodríguez-Villafuerte M. GATE simulation of the intrinsic radioactivity in LYSO scintillation crystals. *Nucl Instrum Methods Phys Res B*. 2019;454:1–5.
18. Enríquez-Mier-y-Terán FE, Ortega-Galindo AS, Murrieta-Rodríguez T, Rodríguez-Villafuerte M, Martínez-Dávalos A, Alva-Sánchez H. Coincidence energy spectra due to the intrinsic radioactivity of LYSO scintillation crystals. *EJNMMI Phys*. 2020;7:21.
19. Jan S, Santin G, Strul D, et al. GATE: a simulation toolkit for PET and SPECT. *Phys Med Biol*. 2004;49:4543–4561.
20. Goertzen AL, Suk JY, Thompson CJ. Imaging of weak-source distributions in LSO-based small-animal PET scanners. *J Nucl Med*. 2007;48:1692–1698.
21. Freedenberg MI, Badawi RD, Tarantal AF, Cherry SR. Performance and limitations of positron emission tomography (PET) scanners for imaging very low activity sources. *Physica Med*. 2014;30:104–110.
22. Wang Q, Mikhaylova E, Baikjiang R, Cherry SR. The reduction of ^{176}Lu background in Lu-based PET scanners using optimized classification. *Phys Med Biol*. 2020;65:175016.
23. Rothfuss H, Panin V, Moor A, et al. LSO background radiation as a transmission source using time of flight. *Phys Med Biol*. 2014;59:5483–5500.
24. Conti M, Eriksson L, Hayden C. Monitoring energy calibration drift using the scintillator background radiation. *IEEE Trans Nucl Sci*. 2011;58:687–694.
25. Cortés-Rodicio J, Sánchez-Merino G, García-Fidalgo MA. Impacto del Lu-176 en el control diario de la resolución energética en un PET/CT con cristales LYSO. *Rev Fis Med*. 2015;16:27–34. <https://revistadefisica.medica.es/index.php/rfm/article/view/182>
26. Knoess C, Gremillion T, Schmand M, et al. Development of a daily quality check procedure for the high-resolution research tomograph (HRRT) using natural LSO background radioactivity. *IEEE Trans Nucl Sci*. 2002;49:2074–2078.
27. Hsu DFC, Freese DL, Reynolds PD, Innes DR, Levin CS. Design and performance of a 1 mm³ resolution clinical PET system comprising 3-D position sensitive scintillation detectors. *IEEE Trans Med Imaging*. 2018;37:1058–1066.
28. Ramirez RA, Zhang Y, Liu S, et al. A lower-cost high-resolution LYSO detector development for positron emission mammography (PEM). *IEEE Trans Nucl Sci*. 2009;56:2621–2627.
29. Springer A, Mawlawi OR. Evaluation of the quantitative accuracy of a commercially available positron emission mammography scanner: quantitative accuracy of a commercially available PEM scanner. *Med Phys*. 2011;38:2132–2139.
30. Raylman RR, Van Kampen W, Stolin AV, et al. A dedicated breast-PET/CT scanner: evaluation of basic performance characteristics. *Med Phys*. 2018;45:1603–1613.
31. Hong KJ, Choi Y, Jung JH, et al. A prototype MR insertable brain PET using tileable GAPD arrays: a MR insertable PET for simultaneous PET/MRI imaging. *Med Phys*. 2013;40:042503.
32. Jakoby BW, Bercier Y, Watson CC, Bendriem B, Townsend DW. Performance characteristics of a new LSO PET/CT scanner with extended axial field-of-view and PSF reconstruction. *IEEE Trans Nucl Sci*. 2009;56:633–639.
33. Jakoby BW, Bercier Y, Conti M, Casey ME, Bendriem B, Townsend DW. Physical and clinical performance of the mCT time-of-flight PET/CT scanner. *Phys Med Biol*. 2011;56:2375–2389.
34. Rausch I, Cal-González J, Dapra D, et al. Performance evaluation of the Biograph mCT Flow PET/CT system according to the NEMA NU2-2012 standard. *EJNMMI Phys*. 2015;2:26.
35. van Sluis J, de Jong J, Schaar J, et al. Performance characteristics of the digital Biograph Vision PET/CT system. *J Nucl Med*. 2019;60:1031–1036.
36. Du J, Schmall JP, Yang Y, et al. Evaluation of Matrix9 silicon photomultiplier array for small-animal PET: evaluation of Matrix9 for small-animal PET. *Med Phys*. 2015;42:585–599.
37. Kim JS, Lee JS, Im KC, et al. Performance measurement of the microPET Focus 120 scanner. *J Nucl Med*. 2007;48:1527–1535.
38. Tai YC, Chatziioannou A, Siegel S, et al. Performance evaluation of the microPET P4: a PET system dedicated to animal imaging. *Phys Med Biol*. 2001;46:1845–1862.
39. Streun M, Brandenburg G, Larue H, Parl C, Ziemons K. The data acquisition system of ClearPET Neuro - a small animal PET scanner. In: 14th *IEEE-NPSS Real Time Conference*, 2005. IEEE; 2005:4 pp. <https://doi.org/10.1109/RTC.2005.1547410>
40. Constantinescu CC, Mukherjee J. Performance evaluation of an Inveon PET preclinical scanner. *Phys Med Biol*. 2009;54:2885–2899.
41. Hallen P, Schug D, Weissler B, et al. PET performance evaluation of the small-animal Hyperion II ^D PET/MRI insert based on the NEMA NU-4 standard. *Biomed Phys Eng Express*. 2018;4:065027.
42. Lage E, Vaquero JJ, Sisniega A, et al. Design and performance evaluation of a coplanar multimodality scanner for rodent imaging. *Phys Med Biol*. 2009;54:5427–5441.
43. Krishnamoorthy S, Blankemeyer E, Mollet P, Surti S, Van Holen R, Karp JS. Performance evaluation of the MOLECUBES β -CUBE—a high spatial resolution and high sensitivity small animal PET scanner utilizing monolithic LYSO scintillation detectors. *Phys Med Biol*. 2018;63:155013.
44. Li X, Alessio AM, Burnett TH, Lewellen TK, Robert S M. Performance evaluation of small animal PET scanners with different system designs. *IEEE Trans Nucl Sci*. 2013;60:1495–1502.
45. Sánchez F, Moliner L, Correcher C, et al. Small animal PET scanner based on monolithic LYSO crystals: performance evaluation: Small animal PET scanner based on monolithic. *Med Phys*. 2012;39:643–653.
46. Moliner L, González AJ, Soriano A, et al. Design and evaluation of the MAMMI dedicated breast PET: design and evaluation of the MAMMI dedicated breast PET. *Med Phys*. 2012;39:5393–5404.
47. Molinos C, Sasser T, Salmon P, et al. Low-dose imaging in a new pre-clinical total-body PET/CT scanner. *Front Med*. 2019;6:88.
48. Benlloch JM, González AJ, Pani R, et al. The MINDVIEW project: first results. *Eur psychiatr*. 2018;50:21–27.
49. Borghi G, Peet BJ, Tabacchini V, Schaart DR. A 32 mm × 32 mm × 22 mm monolithic LYSO: Ce detector with dual-sided digital photon counter readout for ultrahigh-performance TOF-PET and TOF-PET/MRI. *Phys Med Biol*. 2016;61:4929–4949.
50. Eckerman KF, Westfall RJ, Ryan JC, Cristy M. Availability of nuclear decay data in electronic form, including beta spectra not previously published. *Health Phys*. 1994;67:338–345.
51. Basunia MS. Nuclear data sheets for A = 176. *Nucl Data Sheets*. 2006;107:791–1026.
52. Baró J, Sempau J, Fernández-Varea JM, Salvat F. PENELOPE: an algorithm for Monte Carlo simulation of the penetration and energy loss of electrons and positrons in matter. *Nucl Instrum Methods Phys Res B*. 1995;100:31–46.
53. Coursey JS, Schwab DJ, Tsai JJ, Dragoset RA. Atomic weights and isotopic compositions, National Institute of Standards and Technology Data. Published 2015. <http://physics.nist.gov/Comp>
54. XCOM. XCOM: Photon Cross Section Database (version 1.5). National Institute of Standards and Technology, Gaithersburg, MD. Published 2010. <http://physics.nist.gov/xcom>
55. Knoll GF. *Radiation Detection and Measurement*, 4th edn. Hoboken, NJ: John Wiley; 2010.
56. Szczesniak T, Moszynski M, Syntfeld-Kazuch A, Swiderski L, Spurrier Koschan MA, Melcher CL. Timing resolution and decay time of LSO crystals co-doped with calcium. *IEEE Trans Nucl Sci*. 2010;57:1329–1334.

57. Taheri A, Askari M, Taghan SM. Simulation of Gaussian energy broadening in gamma response of a LYSO array detector using a semi-empirical method. *Eur Phys J Plus*. 2017;132:384.
58. Jeong M, Van B, Wells BT, D'Aries LJ, Hammig MD. Comparison between pixelated scintillators: CsI(Tl), LaCl₃(Ce) and LYSO(Ce) when coupled to a silicon photomultipliers array. *Nucl Instrum Methods Phys Res, Sect A*. 2018;893:75–83.
59. MacKay DJC. *Information Theory, Inference, and Learning Algorithms*. Cambridge: Cambridge University Press; 2003.
60. Gonzalez AJ, Berr SS, Cañizares G, et al. Feasibility study of a small animal PET insert based on a single LYSO monolithic tube. *Front Med*. 2018;5:328.
61. Xu J, Xie S, Zhang XI, et al. A preclinical PET detector constructed with a monolithic scintillator ring. *Phys Med Biol*. 2019;64:155009.